Tuning the Activity of Silver Alloys for the Oxygen Reduction Reaction in Alkaline Media

ACS APPLIED ENERGY MATERIALS

www.acsaem.org Article

Tuning the Activity of Silver Alloys for the Oxygen Reduction Reaction in Alkaline Media

Gerard Montserrat-Sisó* and Björn Wickman*

Cite This: *ACS Appl. Energy Mater.* 2023, 6, 6428−6442 Read Online

ACCESS | Metrics & More | Article Recommendations | Supporting Information

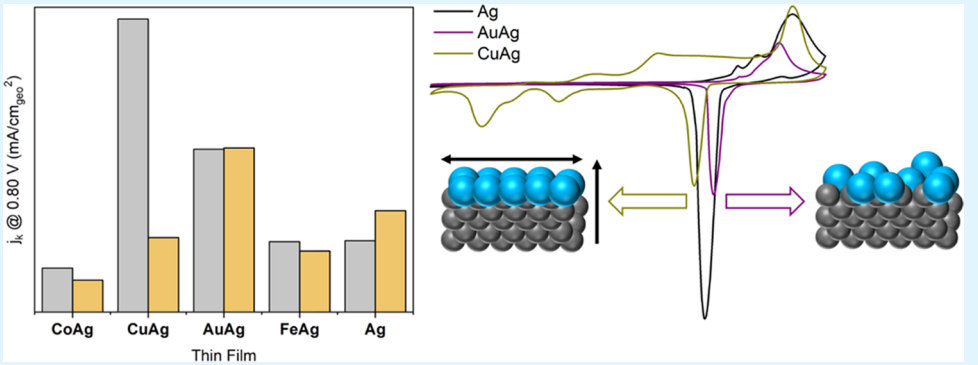

ABSTRACT: Ag-based catalysts have recently attracted much attention as potential candidates to substitute costly Pt-based electrocatalysts for the oxygen reduction reaction (ORR) in alkaline media. Although the electrocatalytic activity of Pt-based alloys is known to exhibit a strong dependence on their electronic structures, a relationship between electronic structure and the ORR mechanism in Ag-based alloys still remains to be elucidated. Herein, by means of physical vapor deposition, we prepare Ag binary thin films (CoAg, CuAg, AuAg, and FeAg) with well-controlled compositions as a tool to investigate the ORR mechanism on Ag surfaces. The bimetallic thin films are evaluated for their ORR performance in alkaline media, and their specific activity at 0.8 V_{RHE} is shown to correlate with the Ag electronic structure. Even though all thin films show different responses to potential cycling, all bimetallic samples exhibit a surface Ag enrichment after ORR. It is shown that the ORR occurs through different mechanisms on these Ag-rich surfaces, which in turn is potential-dependent. Tafel slopes reveal faster ORR kinetics at low overpotentials on all surfaces, whereas only CuAg surpasses pure Ag at higher overpotentials. Moreover, despite their incomplete O_2 reduction, CuAg and AuAg exhibit an overall superior ORR activity over pure Ag, with a more than 2-fold increase in specific activity at 0.8 V_{RHE} attributed to enhancements originating from electronic effects and surface defects, respectively. Since the potential-dependent improved ORR mechanism observed for Ag bimetallic samples makes a rational design of Ag-based electrocatalysts difficult, these results aim to provide insights for a more tailored design of electrocatalysts by shedding light on the mechanisms through which the ORR kinetics are improved on Ag surfaces in alkaline media.

KEYWORDS: *silver, oxygen reduction reaction, electrocatalysis, alkaline fuel cells, thin films, physical vapor deposition*

INTRODUCTION

Increasing demands for lowering anthropogenic CO_2 emissions together with strengthened environmental legislation have resulted in a growing interest in electrochemical devices, among which fuel cells represent a possible net-zero carbon emission power source. Hydrogen fuel cells are of particular interest because H_2 produced by electrolysis with renewable electricity could reduce carbon emissions up to 75%.[1] Moreover, they hold great potential to substitute fossil-powered internal combustion engines, which makes them suitable candidates for the decarbonization of transport systems. Proton exchange membrane fuel cells (PEMFCs) are, due to their high energy density, low-temperature operation, and lightweight, a suitable fuel cell for both light- and heavy-duty transportation.[2] However, the widespread commercialization of PEMFCs in automotive vehicles is currently impeded by their high cost and limited lifetime, which in turn is greatly attributed to the large amounts of platinum needed to catalyze the sluggish oxygen reduction reaction (ORR) kinetics in the cathode.[3] Thus, a large portion of PEMFC research has focused on lowering their cost by decreasing the amount of platinum in the cathode through alloying and microstructuring.[4−6] So far, platinum and platinum

Received: January 26, 2023
Accepted: May 24, 2023
Published: June 7, 2023

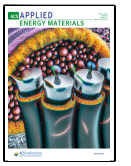

alloys remain as the catalyst benchmark for ORR in acidic media, but their thermodynamic instability in acidic conditions together with their scarcity and high cost demand alternative routes toward precious-metal catalyst eradication.

One of the strategies that have emerged to eliminate costly precious metals is to switch to the alkaline analogue of the PEMFC, the anion exchange membrane fuel cell (AEMFC). Besides the advantages of enhanced ORR kinetics and catalyst stability in alkaline electrolytes, they also bring the possibility for using non-platinum-group metals (PGM) electrocatalysts due to their rather mild alkaline conditions that potentially broaden the spectrum of inexpensive and efficient catalysts. These non-PGM options include doped carbons,[7] transition-metal oxides,[8] and metallic alloys.[9] Among metallic alloys that are stable at a high pH, Ag-based electrocatalysts have attracted much attention due to the high activity of Ag for the ORR under alkaline conditions. Furthermore, Ag is considered one of the few technoeconomical alternatives to Pt for the ORR due to its comparatively low cost and abundance.[10] Other appealing features include high electrochemical stability in alkaline conditions, high complete O_2 reduction selectivity, high electric conductivity, and adequate surface area-normalized turnover frequency.[11,12] However, Ag exhibits the disadvantage of having a specific activity ~1 order of magnitude lower than Pt, as well as a half-wave potential about 200 mV lower than that of Pt-catalyzed ORR.[13,14] Thus, efforts are geared toward improving the ORR activity of Ag to make it competitive with Pt. This often includes engineering the nanostructure to increase its surface area[11,15] or the use of supports such as carbon[16] and metal oxides.[17] A complementary strategy that has been widely used is to increase the intrinsic activity of Ag catalyst through alloying with other metals.[12,18−21] However, the effect of morphology on the activity of these alloys often impedes a correct comparison of activity enhancement mechanisms in different Ag-based transition-metal alloys,[22] which in turn is potential-dependent. Hence, despite the great progress in improving the catalytic activity of Ag-based alloys for the ORR in alkaline media, mechanistic insights of the ORR on Ag surfaces of the same morphology at different potentials remain elusive.

Previous experimental studies have already shown ORR activity enhancement in Ag alloys,[23−25] which has been predicted by means of theoretical modeling based on d-band changes.[26] The dependence of the ORR activity on the energy of the d-band of metals can be elucidated by the mechanistic insight of the reaction. Even though the exact ORR mechanism remains to be elucidated, as in acidic media, it is scientifically accepted that the electrocatalytic reduction of oxygen in alkaline electrolytes can proceed by several pathways, either by a direct $4e^-$ pathway (eq 1)[22]

$$O_2 + 4e^- + 2H_2O \rightarrow 4OH^- \quad (1)$$

which results in the formation of 4 hydroxyl anions, or via the transfer of $2e^-$, which results in the formation of hydroperoxide anion (eq 2)

$$O_2 + 2e^- + 2H_2O \rightarrow HO_2^- + OH^- \quad (2)$$

that can be further reduced by 2 additional e^- (eq 3)

$$HO_2^- + H_2O + 2e^- \rightarrow 3OH^- \quad (3)$$

through the so-called 2 + 2 pathway (eqs 2 and 3). Alternatively, hydroperoxide species can also undergo disproportionation, i.e., without an electron transfer (eq 4)

$$2HO_2^- \rightarrow 2OH^- + O_2 \quad (4)$$

However, the process may be also limited to the formation of hydrogen peroxide, i.e., $2e^-$ pathway. Regardless of which pathway the ORR undergoes, the generation of HO_2^- must be minimized due to its detrimental effect on the fuel cell performance.[27] Regardless of the pathway undertaken by the oxygen molecule, this multistep reaction involves the formation of several oxygenated intermediates, such as O^{2-}, OH^-, O, HO_2^-, and OOH, whose adsorption on the catalytic surface depends on its d-band energy.[28] As indicated by the well-known Sabatier volcano, the fully occupied 5d band in Ag results in a weak binding of oxygenated intermediates.[26] Adsorption of molecular oxygen on the surface is therefore the limiting step in Ag electrodes, although it depends on the overpotential region.[22] Moreover, it has been proposed that the ORR on Ag surfaces proceeds via the $2e^-$ or the $4e^-$ pathway depending on the surface state, which in turn also depends on morphology and electrode potential.[22,29] Since it is highly desirable that the reduction takes place with the complete transfer of 4 electrons, it is of crucial importance that the Ag electrode surface is tuned in order to optimize the ad/desorption ability of Ag sites if its ORR activity is meant to be enhanced. In other words, Ag d-band center must be increased in order to strengthen the Ag−O interaction, leading to easier O−O bond breaking and thus enhancing its ORR kinetics.

Alloying Ag with another metal such as Co, Cu, Pd, or Ni could potentially result in a catalyst with an optimal binding of oxygenated species and thus an improved ORR activity.[21,22,24,25] There are two main mechanisms playing important roles in changing the electronic structure of the host metal upon alloying: ligand and strain effects. The former is observed when the addition of a second metal with a different orbital occupancy induces either an up- or downshift of the d-band center relative to the Fermi level, whereas the latter takes place when the addition of a metal with a dissimilar lattice constant is added, thereby resulting in a broadening or narrowing of the d-band and thus a shift in its center.[30] It must also be mentioned that deconvoluting the interplay between these two effects is often very hard and frequently the "net" d-band center shift is used in rational electrocatalyst design. However, the mixing of two different metals may also result in a third effect that does not necessarily involve alloying: the ensemble effect, in which each metal on the surface plays a different role in the catalytic reaction, thereby promoting a synergetic spillover effect in which surface adsorbed species migrate between different surface sites.[31] Thus, mixing Ag with an oxophilic transition metal could promote the initial O_2 adsorption, whereas Ag would handle the remaining electron transfer steps, thereby enhancing the $4e^-$ pathway through bifunctionality.[32] In closing, for a rational screening of efficient and stable Ag-based electrocatalysts, the understanding of the catalytic mechanism, the catalytic behavior, and the electronic and ensemble effects that play a crucial role in catalyzing the ORR is imperative.

In this work, we use Ag−M bimetallic thin film model systems to investigate the compositional and structural dependence of Ag intrinsic activity for the ORR on Ag-based electrocatalysts. By using Ag-based thin films, the contribution of the morphology effect on the ORR activity is greatly reduced, which enables direct studies of the activity enhancement mechanism, as well as the Ag loading effect. Herein, we deposited Ag onto four different films (Co, Cu, Au, and Fe) and the change in activity due to the underlying film is evaluated in

https://doi.org/10.1021/acsaem.3c00233
ACS Appl. Energy Mater. 2023, 6, 6428−6442

order to elucidate the effect through which the binding energy of reaction intermediates is favorably modified toward the direct $4e^-$ transfer. By means of cyclic voltammetry, X-ray diffraction, and X-ray photoelectron spectroscopy, we report a correlation between the composition and electronic structure of the Ag-rich surface and the ORR route elucidated from monitoring H_2O_2 formation in rotating ring-disk electrode measurements. We show that, despite an uncomplete $4e^-$ O_2 reduction, CuAg and AuAg exhibit an overall enhanced ORR activity compared to pure Ag, although these enhancements were found to be of different origin. More importantly, we demonstrate that the mechanisms that result in improved ORR activities in these bimetallic thin films are highly surface- and potential-dependent and should therefore be addressed individually if each of these is meant to be further improved. Hence, understanding the mechanism behind bimetallic alloy-based enhancements could lead the way for the discovery of structure−activity relationships for more complicated systems, which could potentially give rise to further enhancement of ORR activity on Ag and thus make AEMFCs competitive with current state-of-the-art PEMFCs.

EXPERIMENTAL METHODS

Fabrication of Ag Thin Films. Fabrication of thin films was carried out in cleanroom facilities of Fed. Std. 209E Class 10-100. Bimetallic Ag thin films were deposited onto glassy carbon substrates (5 mm diameter diamond polished Sigradur G disks from HTW Gmbh). The carbon disks were first cleaned by sonication in acetone, isopropanol, and Milli-Q water for 10 min in each solvent followed by plasma cleaning with O_2 at 150 W (Plasma-Therm). Electron-beam evaporation (PVD 225 from Lesker) was used to deposit 40 nm of the underlying metal thin films (i.e., Co, Cu, Au and Fe), after which 4 nm of Ag was sputtered onto the 40 nm metal using DC magnetron sputtering (Nordiko 2000). A potential Ag target oxide layer was removed with 2 min of Ar pre-sputtering. The base pressure of the sputtering system was kept below 1.0×10^{-6} mbar and sputtering was performed in 6.6 mbar under 50 sccm of argon flow. In order to avoid oxidation of the alloying metal in air, the sample transfer time from PVD to Nordiko was kept below 1 min. The PVD was chosen to evaporate the alloying metal due to the availability of materials to be deposited, whereas DC sputtering was chosen to sputter Ag due to its smaller clusters of sputtered material (compared to PVD) and nonlinearity, resulting in an excellent film coverage with the minimum amount of material.[33] The resulting bimetallic thin films were 44 nm in thickness with a Ag loading of 4.2 $\mu g_{Ag}/cm^2$ in all four films, namely, CoAg, CuAg, AuAg, and FeAg. Pure metallic 40 nm samples of Co, Cu, Au, and Fe were fabricated by PVD, whereas the 40 nm Ag samples were fabricated by DC magnetron sputtering.

Electrochemical Measurements. Electrochemical measurements were performed in a three-electrode rotating ring-disk electrode (RRDE) PTFE cell (Pine Instruments) for alkaline electrolytes. The RDE cell was equipped with a graphite rod (Sigma-Aldrich, 150 mm length, 3 mm diameter) as a counter electrode (CE). Graphite was chosen as CE to avoid metal contamination of the working electrode (WE), a very likely event in alkaline electrolytes.[34] A Hg/HgO (1 M KOH) B2220+ Reference Electrode (SI Analytics) was used as a reference electrode (RE). The reliability of the RE was by calibrating before and after each electrochemical test using an RHE (clean Pt wire in H_2-saturated electrolyte) and measuring the intersection of zero current by cycling the potential between −0.02 V and 0.02 V_{RHE} at 2 mV/s. The calibration to 0.00 V_{RHE} was reproducible and around −0.888 V at all times. All polarization measurements were corrected for the uncompensated electrolyte resistance, measured immediately before the polarization measurements by electrochemical impedance spectroscopy. The setup was also equipped with a gas inlet on the side of the cell to allow the electrolyte to be saturated with gasses. The potentiostat used (SP-300 from Bio-Logic) was controlled with the EC-lab software. The samples were mounted on an RDE/RRDE PTFE tip from Pine Instruments using PTFE U-cups. All potentials in this study are potential- and iR-corrected and refer to that of the RHE (V_{RHE}).

The electrochemical cell and glassware were cleaned prior to the measurements in Piranha solution (98% H_2SO_4 (Sigma-Aldrich, EMSURE) and 33% H_2O_2 (VWR Chemicals, Technical), 3:1 v/v) for 24 h. An additional aqua regia cleaning (37% HCl (Supelco, EMSURE) and 65% HNO_3 (Supelco, EMSURE), 3:1 v/v) was carried out after AuAg measurements to ensure the absence of Au traces. The PTFE cell was then thoroughly rinsed with ultrapure water (18.2 MΩ cm, <3 ppb TOC, Milli-Q IQ 7000, Merck) at least 10 times before each measurement. The electrolyte used for ORR measurements consisted of 0.1 M KOH prepared from KOH pellets (KOH hydrate ≥99.995%, Suprapur, Merck) and ultrapure water. The electrolyte was prepared and stored in a PFA volumetric flask (BRAND) to prevent contamination over time from glass corrosion.[35] The Ar used for de-oxygenation of the electrolyte was supplied by AGA with instrument 6.0 purity and O_2 by Strandmøllen (≥99,6 vol %). For surface area determination, $Pb(NO_3)_2$ (99.999%, Sigma-Aldrich) was used.

Two sets of samples were investigated in this study. For one set of bimetallic thin films, the ORR polarization curves were measured directly in as-sputtered thin films. For the other set of bimetallic samples, cyclic voltammetry (CV) at 50 mV/s between 0 and 1 V_{RHE} in Ar-saturated electrolyte was recorded for 25 cycles before the ORR. We observed 25 cycles were enough to reach a stable voltammogram in all samples. The potential window during CV was chosen to not exceed 1.05 V_{RHE} to avoid destructive surface Ag oxidation, which induces roughening.[25] After ORR, another CV under the same conditions was recorded for two cycles to evaluate changes of the surface from ORR. In order to further track any changes in the surface roughness upon ORR measurements, double-layer capacitance measurements between 0.6 and 0.7 V_{RHE} in Ar-saturated were recorded before and after ORR polarization curves. ORR polarization curves were conducted in the same manner for both sets of samples: electrolyte was directly saturated with O_2 for at least 15 min and ORR polarization curves were measured at 50 mV/s in 0.1 M KOH between 0 and 1 V_{RHE} at different electrode rotation speeds varied between 400 and 2500 rpm. We chose this scan rate due to contamination issues, which are more severe at low scan rates in liquid electrolyte.[36] For all ORR polarization curves in both sets of samples, the rotating/ring-disk electrode (RRDE) configuration was used to measure the H_2O_2 generation during ORR. In order to oxidize the H_2O_2 generated at the disk, the potential of the ring electrode was kept at 1.23 V_{RHE}. All samples were stored for <36 h when their electrochemical performance was measured.

The electrochemical surface area (ECSA) of Ag in the bimetallic thin films was measured using Pb underpotential deposition (Pb_{UPD}), a common practice in Ag-based catalysts ECSA determination.[21,29,37,38] For this, the electrolyte was first deoxygenated with Ar for at least 30 min and a 125 μM $Pb(NO_3)_2$ solution was added. To induce the Pb monolayer deposition onto the Ag surface, the potential was held at 0.2 V_{RHE} (slightly above Pb^{2+}/Pb reduction potential) for 300 s and was subsequently scanned to 0.6 V_{RHE} at 10 mV/s to dissolve the underpotentially deposited monolayer, resulting in an oxidative current. The ECSA was then determined by integrating the Pb_{UPD} oxidizing peak and assuming a charge density of 280 $\mu C/cm^2$.[20,39] For CuAg and AuAg samples, the Pb_{UPD} is also active for both Cu and Au, but peak overlapping was dismissed due to the Pb_{UPD} kinetics being much slower on these surfaces and exhibiting stripping peaks at different potentials than that of Ag.[37,40] The ECSA from Pb_{UPD} was measured on as-sputtered samples, after CV, after ORR and after CV + ORR.

Physical Characterization. A PHI 5000 VersaProbe III Microprobe X-ray Photoelectron Spectroscopy (XPS) instrument (Physical Electronics) was used to study the surface composition of the bimetallic thin films. The instrument is equipped with a monochromatic Al K-Alpha X-Ray excitation source (1486.6 eV) operated at 50 W as well as a dual charge compensation: an electron neutralizer (negative charge compensation) and an ion gun (positive charge compensation). Surface composition was evaluated by a survey scan in the binding energy range between 0 and 1400 eV with an energy step width of 0.4 eV. The chemical states of Ag 3d, Co 2p, Cu 2p, Au 4f, Fe 2p, C 1s, and O 1s core-level spectra were studied in the narrow scan, which were recorded

https://doi.org/10.1021/acsaem.3c00233
ACS Appl. Energy Mater. 2023, 6, 6428−6442

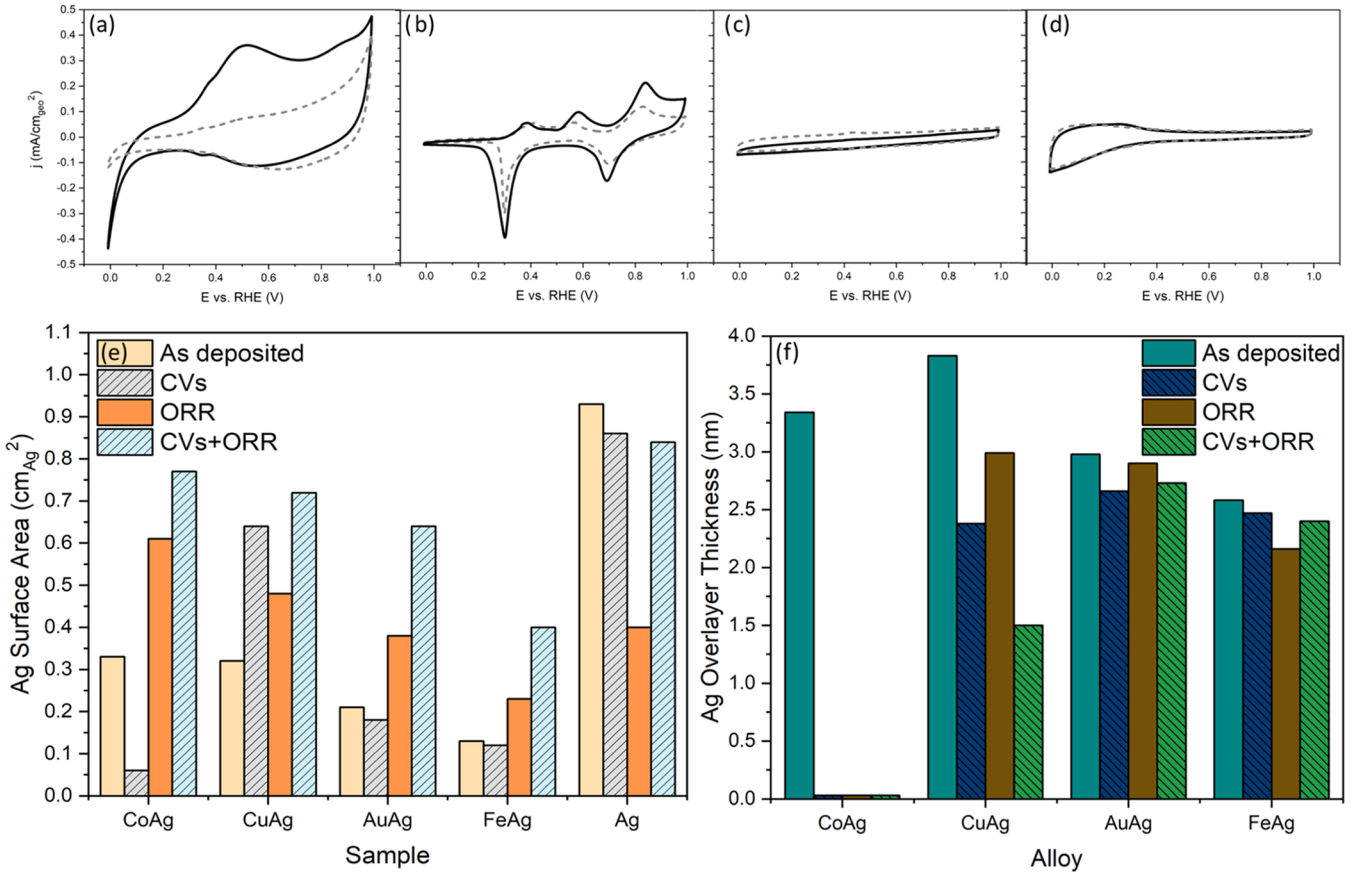

Figure 1. First (solid line) and 25th cycle (dashed line) of CVs performed on as-deposited films of (a) CoAg, (b) CuAg, (c) AuAg, and (d) FeAg at 50 mV/s in deoxygenated 0.1 M KOH. Every thin film had a different response upon both potential cycling and ORR polarization, as evidenced by (e) Ag electrochemical surface areas (ECSAs) of bimetallic thin films before and after both CVs and ORR testing estimated by Pb-stripping. (f) Approximation of the Ag overlayer thickness determined from XPS spectra at 45° and normalized by the maximum information depth.

with an energy step of 0.1 eV and a pass energy of 69 eV. The measuring area was about 200 μm in diameter. The chamber pressure was always lower than 5.0×10^{-9} mbar during measurements. For all samples, the binding energy scale was corrected by shifting the spectra with respect to the adventitious C 1s peak of the C−C bond to 284.8 eV. Angle-resolved XPS was used in the same XPS instrument at three different angles (25, 35, and 45°) and thus three different probing depths in order to measure the surface Ag chemical state more accurately. XPS measurements including angle-resolved XPS were performed for as-sputtered, CV, ORR, and CV + ORR samples. All samples were introduced to the XPS chamber within 12 h after being measured in RDE/RRDE.

Relative sensitivity factors from the PHI-Multipak software were used for the concentration quantification. Concentrations were determined with the effective peak areas after Shirley background subtraction. For the electronic structure and chemical state analysis, the core-level spectra of Ag 3d, Co 2p, Cu 2p, Au 4f, and Fe 2p were curve-fitted with the Multipak software. The fitting routine of the peaks was performed using an asymmetric Gaussian-Lorentzian sum function with a Shirley background. For the Co 2p XPS spectra, the peak associated with the Co $2p_{3/2}$ component of the mixed-valence Co_3O_4 was centered at 780.0 eV, whereas the $Co(OH)_2$ peak was placed at 781.3 eV.[41] Two shake-up satellite peaks were also observed at 786 and 790 eV, corresponding to $Co(OH)_2$ and Co_2O_3, respectively.[41] For the Cu 2p spectrum, the peak observed at 931.8 eV was associated with metallic Cu, the Cu $2p_{3/2}$ peak at 932.5 eV to Cu_2O (Cu^I), and the peak at 934 eV to CuO, whereas the satellites peaks at higher binding energies were ascribed to the characteristic satellites of CuO and Cu_2O.[42] Deconvolution of Au 4f doublet peaks marked the presence of two pairs of bands whose $4f_{7/2}$ peak was centered at 84.0 and 84.9 eV, which were attributed to Au^0 and positively charge Au^+ surface ions, respectively.[43] Lastly, Fe 2p XPS spectra were fitted using Fe^0 (706.8 eV), Fe^{2+} (710.0 eV), and Fe^{3+} (711.8 eV) peaks, together with multiple satellite features observed at higher binding energies arising from Fe oxidized species.[44]

X-ray diffraction (XRD) spectra were collected on a Bruker D8 Discover equipped with a Cu source and an Eiger2 R 500K detector. Measurements were carried out in a Bragg Brentano configuration, with 0.02° step size and 2 s exposure per step. An antiscatter knife was used to eliminate background at low angles, and a motorized primary slit was used to regulate the beam size in order to achieve a fixed sample illumination area during the entire scan. 2.5° Soller slits were used on the source as well as the detector side. A 0.02 mm Ni filter on the source side was used to eliminate K-β radiation.

RESULTS AND DISCUSSION

Two sets of four bimetallic Ag-based thin film samples (CoAg, CuAg, AuAg, and FeAg) were investigated for their electrochemical performance. One set consisted of as-deposited samples in which the ORR activity was measured directly on the Ag overlayer (referred to as "as-deposited" and "ORR" before and after ORR testing, respectively), whereas in the other set of samples, cyclic voltammograms (CVs) were run prior to the polarization curves in order to investigate the ORR after potential cycling, which might induce surface restructuring (referred as "CVs" and "CVs + ORR" before and after ORR testing, respectively).

Cyclic voltammograms run prior to ORR polarization curves were employed to investigate how the surfaces of different bimetallic thin films exhibit different responses upon potential

https://doi.org/10.1021/acsaem.3c00233
ACS Appl. Energy Mater. 2023, 6, 6428−6442

cycling (Figure 1a–d). To further track surface changes induced by electrochemical testing and quantify the Ag surface content, the Ag ECSA was estimated from Pb_{UPD} measurements and was measured in as-deposited samples, samples after running CVs, in ORR, and CVs + ORR samples (Figure 1e). Double-layer capacitance was also measured after CVs (before ORR) and after ORR to gain information on any changes in surface roughness, whose values are reported in Table S1. Moreover, an estimation of the Ag overlayer thickness normalized by the maximum information depth in these four samples was obtained from XPS measurements (Figure 1f), which took into account binding energies, crystal structure, densities, X-ray incident angle, and attenuation length. Details of the Ag thin film thickness calculations can be found in the Supporting Information.

As depicted in Figure 1a–d, the different bimetallic thin films exhibit different responses upon potential cycling, which depends on the oxophilicity of the added metal, as well as on the miscibility and enthalpy of alloy formation of the two metals. The different Ag ECSAs for as-deposited samples, instead, are attributed to the different roughness of the underlying deposited metal (Figure 1e). In the CVs, the potential window was kept below 1 V_{RHE} to avoid destructive surface Ag oxidation, which resulted in Ag features being not observable in the CVs due to its reduction/oxidation taking place above 1 V_{RHE}.[25,45] In the case of CoAg, the voltammograms show the largest difference between the first and last cycle, with one large unpaired peak at 0.5 V_{RHE} (Figure 1a). This is attributed to the presence and/or emerge of the highly oxophilic Co atoms on/into the surface, where they undergo irreversible oxidation to $Co(OH)_2$ and Co_3O_4.[25,46] The initial presence of surface Co in CoAg thin films due to either the incomplete coverage by Ag or the Co atoms emergence between fabrication and RDE testing is corroborated by the broad oxidation peak in the first cycle, whereas the broadening in the last peak confirms the surface Co species still being present after CVs. This is confirmed by the major decrease in Ag ECSA (Figure 1e), whereas the large total surface area estimated from capacitance indicates a surface roughening following CVs. Similarly, CuAg CVs also exhibit peaks characteristic of Cu in both the first and last cycles: three anodic peaks corresponding to Cu oxidation to $Cu(OH)_2$ and Cu_2O, together with the further oxidation to CuO, and two cathodic peaks ascribed to the different reduction steps to back to Cu.[40] Again, this confirms the presence of surface Cu in "as-deposited" CuAg samples at the time of electrochemical testing (Figure 1b). However, the shrinkage of all Cu peaks in the last cycle indicates the disappearance of surface Cu atoms, either due to the retreat into the thin film or the spreading of surface Ag atoms, which increases its ECSA (Figure 1e). More importantly, the CV of pure Cu (Figure S1) exhibits rather different peaks, with a much larger Cu^{I} to Cu^{II} oxidation peak and a Cu^{I} to Cu^{0} reduction peak at a lower potential and higher intensity, indicating both the presence of a more metallic Cu in CuAg and a Cu of different nature than that in pure Cu. AuAg, instead, does not exhibit any Au peak in the cycled potential (0–1 V_{RHE}), so only capacitive currents are observed (Figure 1c).[47,48] Since the total surface area remains close to its ECSA, the increase in the double-layer capacitance region is attributed to the appearance of surface Au, which exhibits reversible OH^- adsorption in this region.[49] However, the emergence of Au into the surface can be considered to be minor due to the slight change in Ag ECSA (Figure 1e). Lastly, FeAg CV exhibits a broad peak at low potentials (0–0.3 V_{RHE}), which is reported to correspond to the formation of $Fe(O)(OH)_x$ species and to be characteristic of oxide-covered polycrystalline iron samples, which is also shown in the pure Fe CV (Figure S1).[50] The hardly noticeable change in its CVs and the constant total surface area are in agreement with the Ag ECSA, which remains almost constant after CVs.

For all samples, a substantial Ag surface enrichment after ORR measurements is observed, which is even more pronounced for CVs + ORR samples (Figure 1e). For ORR samples, the Ag ECSA after ORR testing is between 1.5 and 2 times larger than that of as-deposited samples, whereas for samples in which CVs have been run prior to the ORR (CVs + ORR), the ECSA increase ranges from 1.2- to 13-fold increase compared to the Ag ECSA after only CVs for CuAg and CoAg, respectively. This phenomenon has been observed in both experimental and theoretical studies of many Ag-based bimetallic alloys upon electrochemical cycling in O_2-saturated electrolytes.[18,51,52] The reason behind the different surface Ag increase on different samples can be explained in terms of both surface energies, which in turn depends on crystal structure, and the oxophilicity of the different metals. In all samples considered, the surface energy of the alloying metal is always larger than that of Ag, indicating that the Ag enrichment on the surface is thermodynamically favored.[53] For CoAg and FeAg, both host metals exhibit a different crystal structure than Ag (hcp and bcc vs fcc), which results in a system where the formation of an alloy is more thermodynamically hindered and thus a more heterogeneous surface is formed. For the case of CuAg and AuAg, both metals exhibit an fcc structure and, although their Ag enrichment could also be explained in terms of lower surface energies, it has been speculated that the formation of a surface enriched with the less abundant element is driven by entropy.[54] The different metals' oxophilicity also plays a role in the final surface Ag content. Since the less noble metals will tend to oxidize in the presence of O_2, there could be a driving force at positive potentials to form a surface oxide, which requires the emergence of the underlying metal to the surface and thus a decrease in Ag ECSA. Although the overall surface Ag enrichment in ORR bimetallic samples is justified by the differences in surface energies, the further increase in Ag ECSA in all samples when CVs are recorded prior to the ORR measurements cannot be explained in terms of surface energies or oxophilicity. Instead, this phenomenon is associated with an activation process taking place upon potential cycling, which presumably increases the stability and reorganization of Ag surface atoms.[55,56] As expected, pure Ag thin films exhibit the largest Ag ECSA among all samples, which is maintained through electrochemical measurements. However, it was noted that the measured Ag AECSA was largely reduced for the sample with only ORR measurements. It is likely that the decrease in Ag ECSA for the pure Ag sample after ORR arises due to a reorganization of the surface toward a more thermodynamically stable surface in those conditions, which is different than that of bimetallic samples due to the absence of a second metal that undergoes oxidation/reduction in the potential range considered.

The mobility of Ag atoms across and along the thin film can be better understood with their Ag overlayer thickness, which was estimated from XPS assuming a homogeneous discreet Ag film with a well-defined crystal structure (Figure 1f). The relation between the Ag ECSA and the thickness of the Ag overlayer can provide insights into both overlayer homogeneity and thin film roughness. Again, the different thicknesses in as-deposited samples can be ascribed to the different roughness of the

https://doi.org/10.1021/acsaem.3c00233
ACS Appl. Energy Mater. 2023, 6, 6428–6442

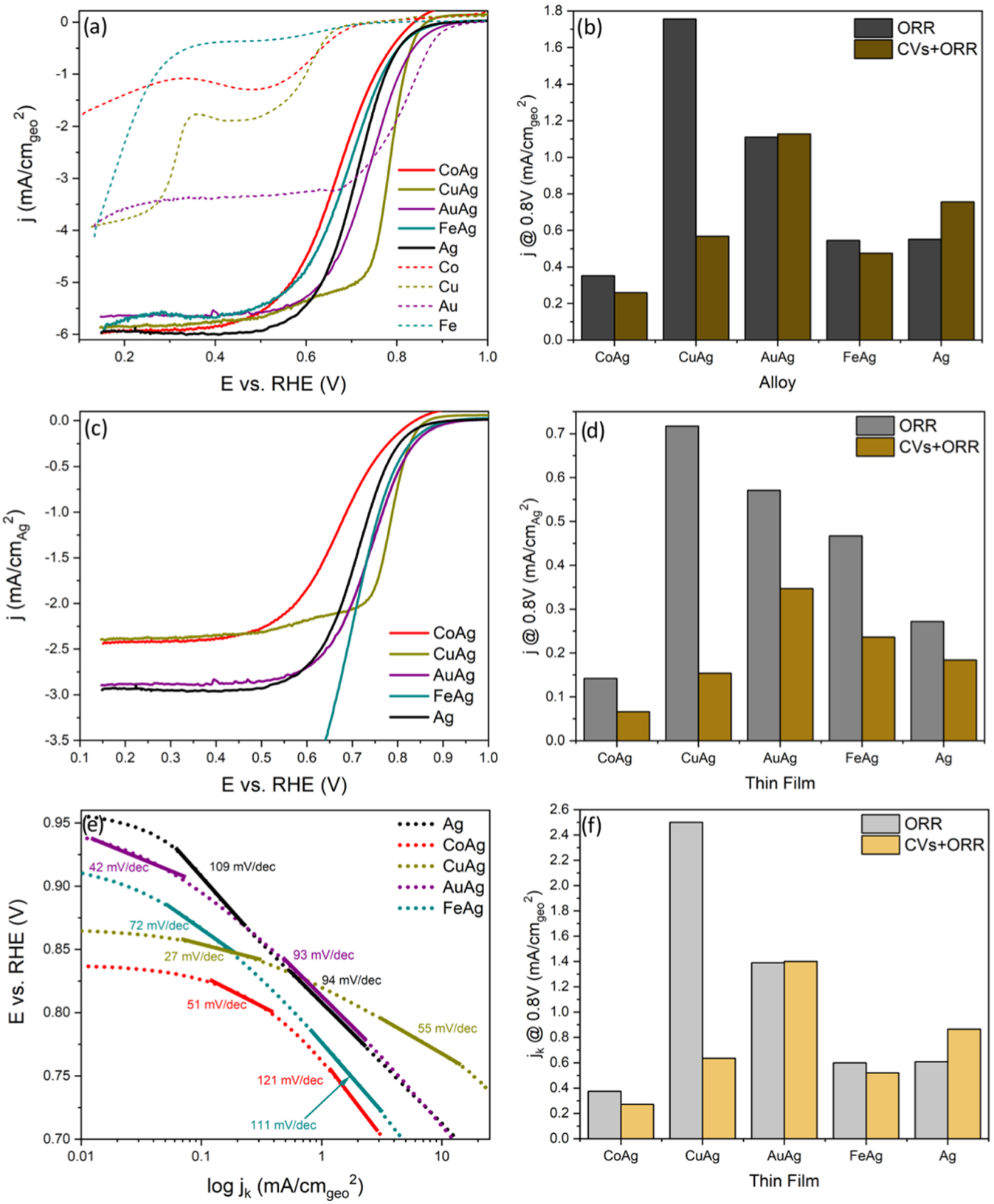

Figure 2. (a) ORR geometric current densities of ORR samples of Ag bimetallic thin films and of pure metals in 0.1 M KOH and (b) geometric current densities of both ORR and CVs + ORR bimetallic samples at 0.80 V_{RHE}. (c) ORR specific current densities normalized by the Ag ECSA estimated using Pb_{UPD} for Ag bimetallic thin films at 1600 rpm and (d) specific current densities of both ORR and CVs + ORR bimetallic samples at 0.80 V_{RHE}. (e) Tafel plots and Tafel slopes of ORR samples and (f) geometric kinetic currents at 0.80 V_{RHE} obtained from the Levich equation. This potential has been chosen for a reliable activity comparison to ensure all samples were found at the kinetic and mass transport mixed region. The geometric and specific current density plots of CVs + ORR samples are found in the Supporting Information (Figures S2 and S3).

https://doi.org/10.1021/acsaem.3c00233
ACS Appl. Energy Mater. 2023, 6, 6428−6442

underlying films. Even though CoAg ORR and CVs + ORR present the largest Ag ECSA, all CoAg samples exhibit an almost nonexistent Ag overlayer after electrochemical testing, which is ascribed either to an emergence of Co atoms during the time between RDE and XPS measurements due to their high oxophilicity and/or to the heterogeneous nature of surface Ag. CuAg samples show the largest difference in Ag overlayer thickness upon electrochemical cycling, with a rather smooth thin Ag overlayer after ORR and a rough, thick layer after CVs + ORR. Both AuAg and FeAg, instead, exhibit a rather constant Ag thin film thickness throughout the electrochemical test, despite the large difference in their ECSAs, which indicates a rather stable homogeneous surfaces with a variable roughness, as inferred by their invariant CVs.

The electrocatalytic ORR polarization behaviors of the Ag-based thin film catalyst were evaluated in O_2-saturated 0.1 M KOH using an RRDE setup. Polarization curves of geometric ORR currents (Figure 2a) revealed rather similar electrochemical responses to applied potential, with all bimetallic samples exhibiting similar limiting current densities. However, they present a comparatively wide range of onset potentials and ORR geometric activities, with two bimetallic samples exhibiting superior geometric activity compared to Ag 40 nm: CuAg and AuAg, which both contain 10 times less Ag than the pure Ag reference sample. For CuAg, the onset potential is lower than that of Ag (0.87 V_{RHE} vs 0.93 V_{RHE}), but the activity trend quickly reverses at 0.82 V_{RHE} and thereafter becomes greater at all potentials considered, with the highest activity enhancement at 0.65 V_{RHE}. The beneficial effect of alloying is therefore most noticeable in CuAg, which shows an overall better ORR performance than Ag and also Cu, which exhibits a high-onset 2 + $2e^-$ pathway that reduces hydroperoxide only at potentials beyond 0.3 V_{RHE}. AuAg, in contrast, does exhibit a better onset potential than Ag (0.94 V_{RHE}), although is still lower than that of pure Au (0.97 V_{RHE}), which exhibits an either $2e^-$ or a 2 + $2e^-$ pathway.[48,57] However, the resulting combination of these two noble metals somehow gives rise to a catalyst with a seemingly improved $4e^-$-driven ORR performance that is unfailingly higher than Ag in all kinetic potentials. The enhancement role of the added metal is most noticeable for CoAg samples, which exhibited the lowest geometric current densities and onset potential (0.83 V_{RHE}) despite having the largest amount of surface Ag. This is somewhat predictable given the activity of pure Co, which exhibits the second lowest activity as a result of $2e^-$ hydroperoxide production. Similarly, despite having a reasonable onset (0.88 V_{RHE}), FeAg thin films were found to show an inferior ORR activity to Ag, which further diverges from Ag with increasing overpotential.

Geometric activities at 0.80 V_{RHE} have been compared for both ORR and CVs + ORR samples (Figure 2b). As explained above, only the addition of Cu and Au resulted advantageous in ORR activities, with a 3- and 2-fold increase at 0.80 V_{RHE}, respectively. Although all bimetallic samples exhibited a further Ag surface enrichment when CVs were run prior to the ORR (Figure 1e), the geometric activities of CVs + ORR samples indicated an overall decrease in ORR activities when more Ag was present on the surface. CuAg CVs + ORR exhibited a substantial decrease in ORR geometric activity compared to CuAg ORR, only surpassing Ag in a short potential range between 0.65 and 0.78 V_{RHE} and showing an even lower onset and limiting current density (Figure S2). The emergence of Co during CVs is reflected in the activity of CoAg CVs + ORR, which at low overpotentials behaved as CoAg ORR and substantially decreased its activity as potential is swept. The activities of both AuAg and FeAg, instead, were unexpectedly similar for their ORR and CVs + ORR samples at all overpotentials, indicating an electronically similar and stable surface upon potential cycling regardless of previous electrochemical cycling. Thus, except for AuAg and FeAg, initial potential cycling does induce surface composition variations that affect their ORR performance.

ECSA is a valuable surface parameter to track surface modifications and evaluate Ag utilization, as it depicts the intrinsic activity of active sites. Specific current densities for ORR and specific activities at 0.80 V_{RHE} for both ORR and CVs + ORR samples are shown in Figure 2c,d, respectively. At low overpotentials, two well-separated current−potential responses can be observed in Figure 2c: a set of samples that exhibit a distinctly enhanced ORR specific activity compared to Ag (FeAg, CuAg and AuAg), and CoAg that present a low ECSA-normalized activity. Evidently, the poorer specific activity of Ag is attributed to its large amount of surface Ag, whereas CoAg reflects the unimprovement of Ag intrinsic activity by Co atoms. Hence, the beneficial effect of a second metal addition is evident for CuAg, AuAg, and FeAg samples, which displayed more than 2-fold specific activity increase with respect to pure Ag at 0.80 V_{RHE} (Figure 2d). If the potential is cycled prior to ORR measurements, although the trend is rather maintained, the observed specific activities are significantly lower than that of ORR samples. This is attributed to the larger Ag surface enrichment on CVs + ORR samples that brings enough Ag to the surface to attenuate the effect of the underlying metal, which is most noticeable for CuAg. Thus, specific activities demonstrate that the overall performance was strongly influenced to a different extent by the presence of a second metal.

In order to further elucidate the detrimental or beneficial effect of alloying Ag with other transition metals and gain insights on the ORR mechanism in Ag bimetallic samples, Tafel plots and kinetic current densities at 0.80 V_{RHE} for ORR samples are shown in Figure 2e,f, respectively. For most samples, two different linear current−potential regions were considered for the Tafel analysis: close to E_{onset} and ∼100 mV from E_{onset}. All bimetallic samples show a remarkable change in Tafel slope when going to higher overpotentials and, although the exact mechanistic change is difficult to identify by Tafel analysis due to the multistep nature of the ORR, this indicates intrinsic changes in the rate-determining step (RDS), the electronic structure of the active sites and/or adsorbates.[58] Regardless, the remarkably lower observed Tafel slope for all bimetallic samples in the activation control region demonstrates the enhanced intrinsic ORR kinetics on these samples with respect to pure Ag, whose rather high Tafel slope indicates that the first electron transfer step to $O_{2,ad}$ is the RDS.[12,59] Both Tafel slope values found for Ag are within previously reported Tafel slopes for polycrystalline Ag surfaces in alkaline solutions, which are proposed to be highly surface-dependent.[12] At low-current densities, CuAg shows a strikingly low Tafel slope of 27 mV/dec, which is by far the lowest among all samples. This is in good agreement with its outstanding geometric, specific, and kinetic current densities and demonstrates a significantly higher ORR reaction rate with the chemical step after the first electron transfer as the RDS, i.e., OOH formation.[60] In the same region, AuAg shows the second lowest slope (42 mV/dec), followed by CoAg (51 mV/dec) and FeAg (72 mV/dec), which is also rather concomitant with their kinetically corrected currents (Figure 2f). More importantly,

https://doi.org/10.1021/acsaem.3c00233
ACS Appl. Energy Mater. 2023, 6, 6428−6442

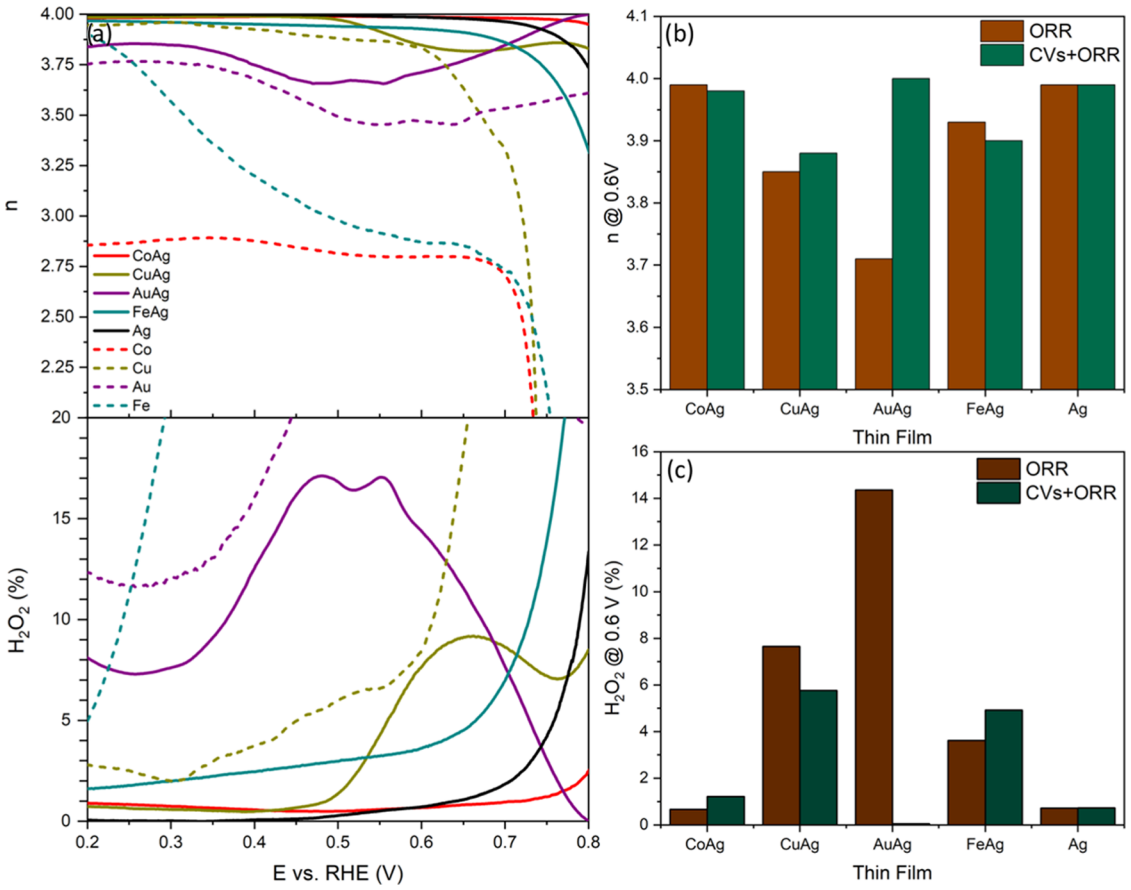

Figure 3. (a) Electron transfer coefficients (n) of bimetallic and pure metal ORR samples determined in RRDE measurements in 0.1 M KOH (top) and the corresponding hydroperoxide formation percentage for the same samples (bottom). (b) Electron transfer coefficients at 0.6 V_{RHE} for both ORR and CVs + ORR samples and (c) hydroperoxide formation of the same samples at 0.6 V_{RHE}.

whereas the significantly lower Tafel slopes observed for bimetallic samples at low overpotentials indicate a prominent enhancement of ORR kinetics, their notably larger Tafel slopes at higher overpotentials resemble that of Ag, indicating a mechanism controlled by the first electron transfer in all samples except CuAg. At this region, only CuAg exhibits improved ORR kinetics compared to pure Ag (55 mV/dec vs 94 mV/dec), which suggest a more favorable oxygen binding energy, whereas AuAg shows a very similar slope at the same potential (93 mV/dec). Thus, given the different slopes observed at higher currents, we infer that the first step in the ORR mechanism is of different nature on all surfaces due to the different OH^- and O adsorption energies, which can exhibit a potential-dependent site-blocking effect and thus hinder complete O_2 reduction to OH^-.[61] The kinetically corrected currents also reflect the remarkably better performance of CuAg and AuAg in catalyzing the ORR, which exhibit a 4- and 2-fold enhancement, respectively (Figure 2f). Moreover, whereas AuAg CVs + ORR maintains an enhanced kinetic current, it seems that the ORR kinetics are significantly weakened for CuAg CVs + ORR, which contains much less surface Cu than CuAg ORR. Pure Ag kinetically corrected current also presents enhanced activity after CVs, indicating the role of crystal planes and/or surface defects in its ORR kinetics. Overall, the observed Tafel slopes at low currents and the generally large kinetic current densities suggest an either direct (eq 1) or indirect (eqs 2 and 3) $4e^-$ ORR pathway at low overpotentials for all samples.

Since hydrogen peroxide (H_2O_2) can be formed as a side product for ORR, rotating ring-disk electrode (RRDE) measurements were performed to monitor the peroxide fraction and the electron transfer number (n) through potential cycling. Figure 3a depicts both the n (top) and the peroxide fraction (bottom) of all bimetallic thin films as well as pure metallic films between 0.20 and 0.80 V_{RHE}, whereas Figure 3b,c shows the n and H_2O_2 formation, respectively, at 0.60 V_{RHE} for all samples. The complete range of n and H_2O_2 formation for all samples is found in Figure S4. As observed, all bimetallic samples present a lower H_2O_2 formation than the pure host metals and thus a higher electron transfer number in all potentials considered, indicating either a direct (eq 1) or indirect (eqs 2 and 3) $4e^-$ pathway (n > 3.7). However, only CoAg exhibits selectivity toward H_2O formation comparable to that of Ag, which exhibits a complete $4e^-$ O_2 reduction at high overpotentials and thus indicates that the Ag-O_{ad} interaction is enough to break the O−O bond. This is somewhat surprising given the poor activity of Co toward catalyzing the complete O_2 reduction to H_2O, most likely due to the presence of low valence Co oxides that catalyze both the $2e^-$ (eq 2) and the $2 + 2e^-$ pathway (eq 3).[62] This could indicate the presence of ensemble effects in CoAg, in which Co species facilitate the initial oxygen binding and Ag atoms help to desorb the resulting OH^-. Despite the improved activities and low Tafel slopes that were observed for both CuAg and AuAg, RRDE measurements revealed the existence of a $2e^-$ pathway taking place on these surfaces. AuAg shows the largest H_2O_2 formation among all bimetallic samples, up to 20 times higher

https://doi.org/10.1021/acsaem.3c00233
ACS Appl. Energy Mater. 2023, 6, 6428−6442

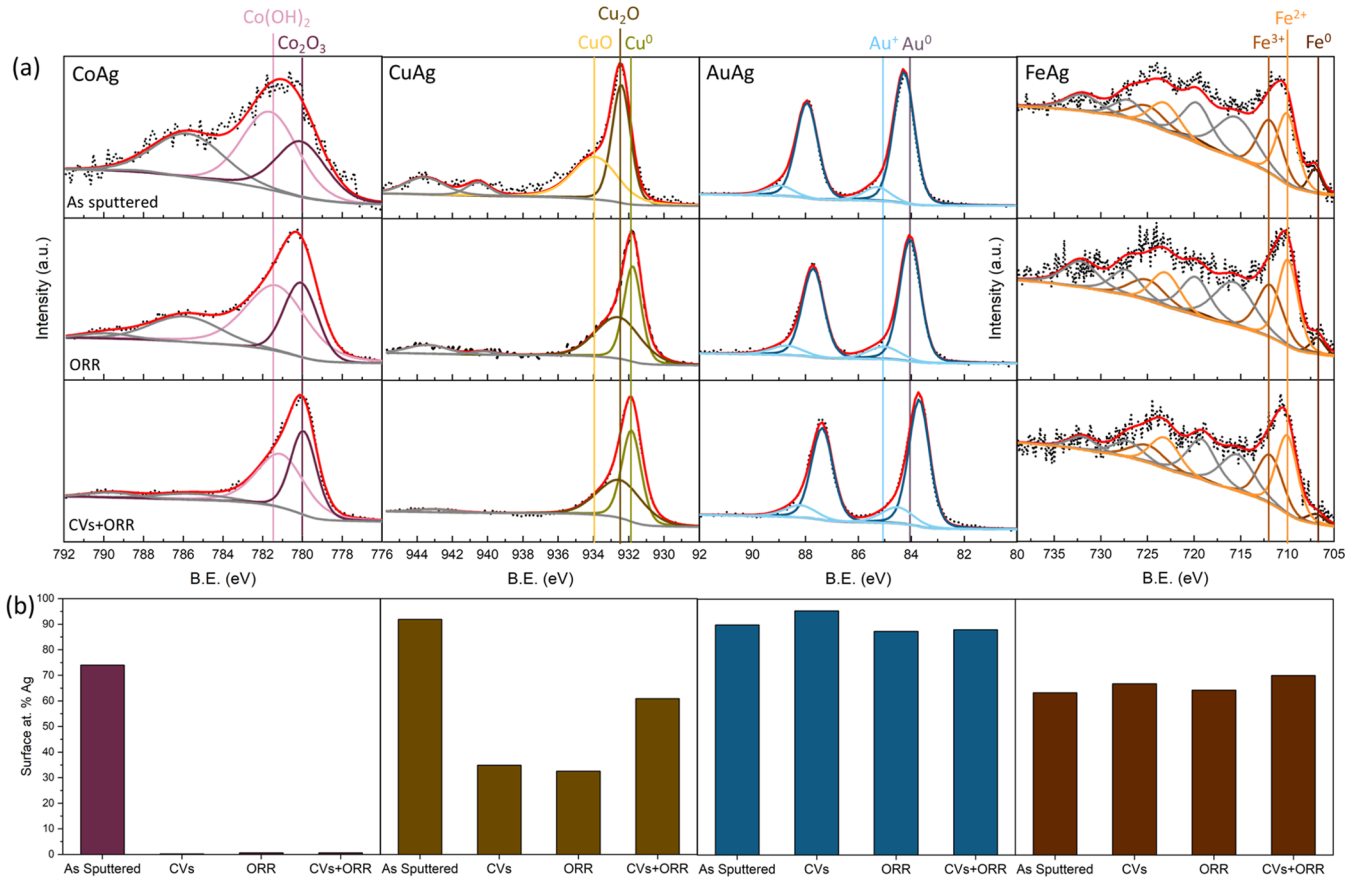

Figure 4. (a) XPS deconvoluted spectra of Co 2p, Cu 2p, Au 4f, and Fe 2p in bimetallic thin films for as-sputtered (top), ORR (middle), and CVs + ORR (bottom) measured at 45°; (b) surface atom % of Ag for as-sputtered, after CVs, after ORR and after CVs + ORR samples of bimetallic thin films measured in XPS at 25°.

than that produced by pure Ag at 0.6 V_{RHE}. However, the dominance of the $2e^-$ pathway in AuAg is seemingly very dependent on the potential region, where it reaches a maximum H_2O_2 production of 17% close to 0.5 V_{RHE}. Interestingly, AuAg CVs + ORR exhibits the exact same behavior but starting at higher overpotentials (from 0.48 V_{RHE}) and presenting a complete O_2 reduction to H_2O until then (Figure S4). This could be attributed to a presumably higher presence of surface Au that emerges at certain potentials and fails to further reduce HO_2^- to H_2O at the potential range considered, as evidenced by its much larger ring currents, which in turn is ascribed to an irreversible OH^- adsorption that block the surface for the two-site O_2 adsorption required for the direct $4e^-$ ORR.[29] Regardless, the strong presence of the $2e^-$ pathway in AuAg is somewhat surprising given the large currents generated at a rather wide potential range (Figure 2). CuAg, although it also exhibits a H_2O_2 production apex between 0.50 and 0.75 V_{RHE}, its bump is concomitant with the sudden change of trajectory when entering the diffusion-controlled region in its geometric currents (Figure 2). Interestingly, this potential is in very good agreement with the potential of Cu oxidation to Cu_2O, which is inactive in catalyzing the ORR and whose formation starts with the adsorption of hydroxide species that would potentially hinder the O_2 two-site adsorption and thus facilitate H_2O_2 formation.[24] Moreover, CuAg CVs + ORR also presents the same low n region starting from 0.34 V_{RHE}, which may indicate a more facile $Cu(OH)_2/Cu_2O$ formation. The third less efficient thin film to catalyze the complete O_2 reduction is FeAg, whose H_2O_2 production also exhibits an exponential behavior as Ag and reaches its minimum at 0.20 V_{RHE} (<2%). As in CoAg, the low H_2O_2 production observed in FeAg is rather unexpected given the poor activity of pure Fe, whose ORR seemingly proceeds partially via the $2e^-$ route at low overpotentials and approaches $4e^-$ when decreasing potential. Thus, given that its ring currents exhibit a near-parallelism with that of pure Ag, we infer that the peroxide formation on this bimetallic surface is merely dependent on the amount of surface Ag that catalyzes the $4e^-$ pathway. FeAg CVs + ORR, instead, revealed the presence of $2e^-$-driven oxide-covered Fe on the surface at potentials above 0.3 V_{RHE} (Figure S5). The selectivity to H_2O for all Ag-based thin films was also assessed with the Koutecky–Levich analysis at 0.60 V_{RHE} (Table S2) and found that the number of electrons transferred is between 3.5 and 4, indicating the virtually complete reduction of O_2 to H_2O in these catalysts. The n values calculated in the Koutecky–Levich analysis correlate well with the ones found in RRDE. Moreover, all thin films exhibit good linearity between current density and rotation speed, as well as near-parallelism, suggestive of first-order reaction kinetics with respect to dissolved O_2. Nevertheless, a precise comparison of H_2O_2 production on different bimetallic catalysts is rather difficult due to their changes in surface crystal planes and compositions upon potential cycling.

X-ray photoelectron spectroscopy (XPS) was used to track changes in both surface composition and the binding energy of Ag upon electrochemical testing. Figure 4a depicts the deconvoluted XPS spectra for the different alloying metals

https://doi.org/10.1021/acsaem.3c00233
ACS Appl. Energy Mater. 2023, 6, 6428−6442

(Co 2p, Cu 2p, Au 4f, and Fe 2p) for as-sputtered thin films (top), after ORR (middle) and after CVs + ORR (bottom), whereas Figure 4b shows the changes in surface Ag after different electrochemical tests. As expected, the XPS spectra of Co do not show any metallic Co, even for the as-sputtered film (Figure 4a). Instead, the spectra reveal the presence of both $Co(OH)_2$ and the mixed-valence spinel oxide Co_3O_4, which increases after electrochemical testing, especially for ORR. Although Figure 4b evidences the major Co surface enrichment after applying potential (i.e., absence of surface Ag), the Ag ECSA discloses the presence of surface Ag after testing (Figure 1e). We attribute this disagreement to either the emergence of the highly oxophilic Co atoms between testing and XPS analysis or to the presence of a very thin Ag film. In either case, both geometric and specific activities evidence the unsuccessful alloying between Co and Ag that has previously been shown to enhance Ag intrinsic activity.[25,63] We therefore assign the better selectivity of CoAg toward H_2O formation at some potentials (Figure 3a) to the larger presence of the high-valence oxide (Co_3O_4), which is known to promote the $4e^-$ route,[62] whereas we attribute the higher activity of CoAg CVs + ORR merely to a larger surface Ag content. Taken together, these results show that surface ligand effects do not play a role in catalyzing the ORR in the CoAg surface; that is, Co oxides and Ag in close proximity are no better than pure Ag.

The Cu XPS spectra in CuAg also present changes in the surface Cu species after RDE testing, with the as-sputtered film exhibiting only Cu oxides (Cu_2O and CuO) and CuAg after ORR showing both Cu^0 and Cu_2O (Figure 4a). This is in good agreement with both in situ and theoretical studies that reported a higher Cu oxidation resistance in CuAg than in Cu alone, which is only active for the ORR as Cu^0, and presumably gives rise to the activity enhancement in the reduced Cu potential region.[64] Moreover, it should also be mentioned that, although there is no Cu^0 in the as-sputtered CuAg film to compare binding energies with, the value of the Cu^0 $2p_{3/2}$ peak centered at 931.8 eV in after-ORR samples is significantly lower than those reported in the literature,[42,65] which could indicate a change in Cu electronic structure that results in a weaker O_{ad} and thus a better ORR intrinsic activity. This is in good agreement with previous studies on the same bimetallic samples, which claim that the enhancement is due to electronic effects, in which either Ag weakens Cu oxygen binding energy[24] or Cu tunes Ag d-band center toward better oxygen adsorption.[16] On the other hand, the distinctly better CuAg ORR performance compared to CuAg CVs + ORR observed in Figure 2 could be explained in terms of the surface Cu/Ag ratio, which has been determined to be 68:32 in XPS (Figure 4b) and correlates very well with the previously reported optimal $Cu_{70}Ag_{30}$ surface ratio for catalyzing the ORR in alkaline media.[64] However, there is a vast amount of Ag/Cu surface ratios that have been reported to be optimal catalysts for the ORR,[16,18,66] although the difference in ORR activities of CuAg catalysts may result from different morphologies or crystal structures. Another plausible explanation could be ensemble effects, in which Ag takes care of OH^- desorption, whereas Cu handles the first oxygen adsorption. In any case, since a better OH^- desorption by Ag and an enhanced O_{ad} by Cu would result in an optimal bifunctional effect, we conclude that electronic and ensemble effects combined would give rise to the utmost activity enhancement and therefore they do not have to be ruled out by each other.

XPS on AuAg samples revealed a surprisingly stable bimetallic system in terms of both Au species (Figure 4a) and surface composition (Figure 4b), which is concomitant with their almost identical ORR activities (Figure 2). Deconvolution of Au 4f XPS spectra shows a constant and insignificant amount of positively charged Au^+ before and after RDE tests. More importantly, there is a major core-level downshift in the Au 4f spectra of AuAg samples after ORR. Although this could indicate a final state effect that shifts down the measured binding energy,[43] we attribute this shift toward lower binding energies to either a downshift of its d-band center toward the Fermi level and/or the presence of surface undercoordinated Au atoms.[67] The reason for the dismissal of Au surface atoms with different surface energy is due to the absence of surface Au. Thus, the higher surface energy of Au that results in a thermodynamically driven surface enrichment of Ag suggests the absence of ensemble effects in AuAg.[22] This is further proven by the highly steady surface composition found in XPS (Figure 4b), together with the unchanging Ag thin film thickness (Figure 1e), which evidences the absence of Au and Ag intermixing in the surface. It is also plausible that Au emerges to the surface at certain potentials, which would explain the rather large H_2O_2 production in Figure 3 at specific regions and most likely differs from that of AuAg CVs + ORR due to different system thermodynamics induced by the precedent CVs. However, the Ag ECSA determined in Figure 1e suggest the reorganization of surface Ag atoms after potential cycling. For this reason, we attribute the enhanced ORR kinetics of AuAg to either surface defects, which would result in both increased ECSA and a higher number of low-coordinated Ag atoms and/or an upshift of Ag d-band center, since both effects may facilitate the chemisorption of O* and potentially enhance the ORR on the pure Ag surface. The presence of surface structural defects, such as crystalline boundaries, can serve as excellent catalytic sites owing to the enriched surface electronic states and shifted d-bands, which favor the OH^- adsorption.[57] Hence, a large presence of undercoordinated Ag atoms in edges and vertices results in a less reversible OH^- adsorption, which may hinder the two-site O_2 adsorption needed for the complete $4e^-$ reduction and therefore generate more H_2O_2, which is in accordance with the RRDE results observed in Figure 3a.

Similarly, the Fe 2p XPS spectra in FeAg also exhibit a constant ratio of Fe species throughout electrochemical testing, largely consisting of Fe^{2+} and Fe^{3+} species. In contrast to other samples, the deconvoluted Fe^0 spectra do not show any significant changes in its binding energy, thereby evidencing the unchanged electronic structure of Fe during RDE testing. Moreover, as in AuAg, both the XPS quantification (Figure 4b) and the Ag thin film thickness in FeAg (Figure 1f) indicate a surprisingly stable Ag overlayer upon potential cycling, which explains the very similar geometric and kinetic currents observed for FeAg ORR and FeAg CVs + ORR in Figure 2, which are both very similar to that of pure Ag. Correspondingly, peroxide formation on FeAg ORR surface (Figure 3a) reveals a surface very similar to Ag although slightly less active in catalyzing the complete O_2 reduction, most likely due to the lower amount of Ag. In FeAg CVs + ORR samples, instead, the RRDE measurements revealed a Fe-like behavior, suggesting that the CVs prior to ORR facilitate the emergence of Fe at those potentials. Although previous research has demonstrated the beneficial synergetic effect resulting from a Ag−Fe nanostructure,[68] we conclude that the structure presented in this work fails to induce electronic modifications in the Fe−Ag system that would result in enhanced ORR kinetics.

https://doi.org/10.1021/acsaem.3c00233
ACS Appl. Energy Mater. 2023, 6, 6428−6442

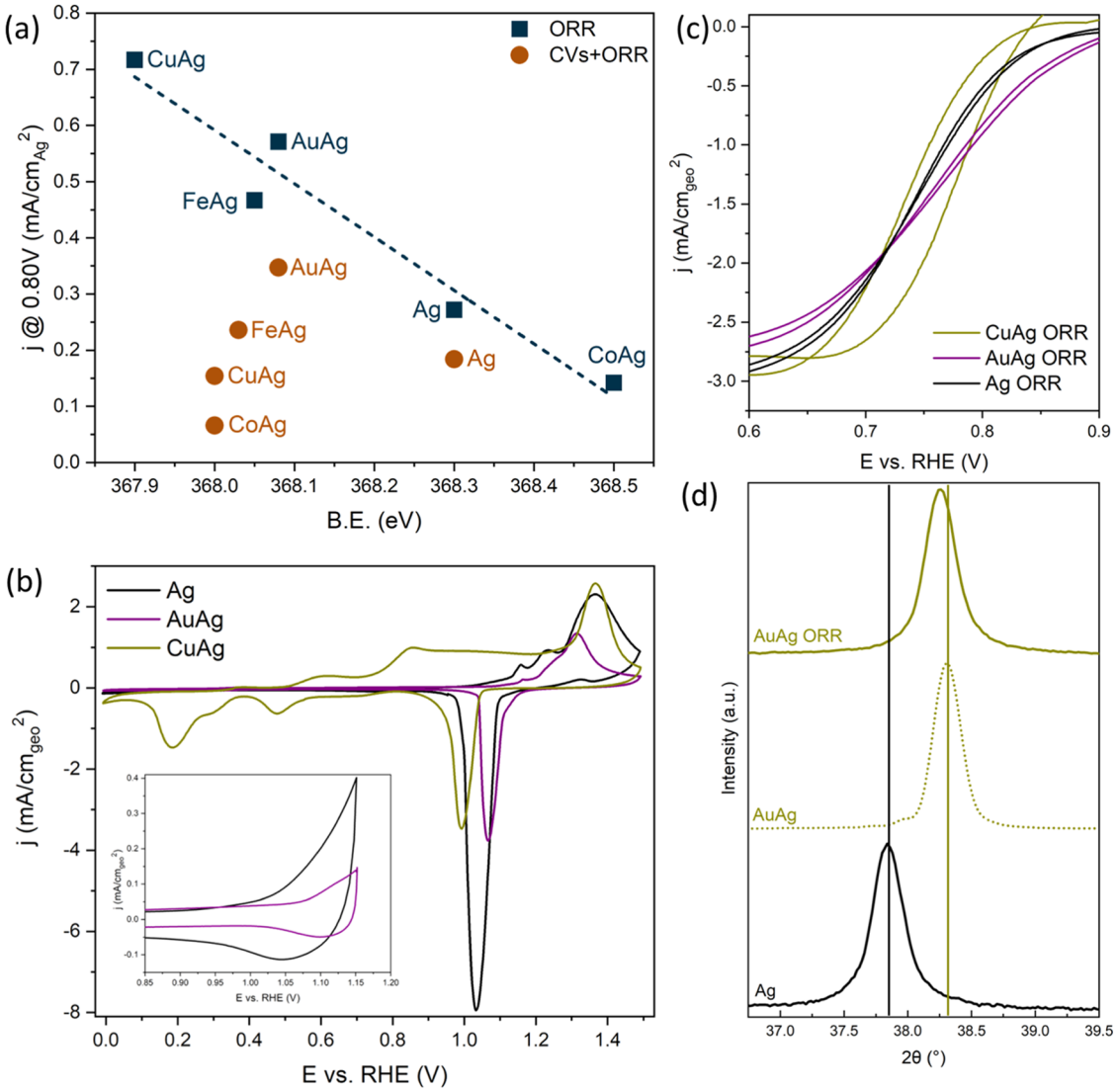

Figure 5. (a) Correlation between the binding energy of Ag in bimetallic thin films and pure Ag measured in XPS at 25° and their specific activities at 0.80 V_{RHE}; (b) cyclic voltammograms at 0−1.5 V_{RHE} of CuAg ORR, AuAg ORR, and Ag ORR in Ar-saturated 0.1 M KOH and (inset) CVs of AuAg and Ag between 0.85 and 1.15 V_{RHE}; (c) anodic and cathodic polarization curves of Ag ORR, CuAg ORR, and AuAg ORR 400 rpm; and (d) XRD patterns of Ag and AuAg as-sputtered and AuAg ORR.

To further deconvolute the interplay between the different effects playing a role in boosting Ag-based thin films ORR activity, specific activities at 0.80 V_{RHE} were plotted against Ag binding energy (Figure 5a). As shown, there is a strong correlation between Ag binding energy and the observed specific activity for ORR samples, which in principle could indicate that the d-band center of Ag is the main descriptor for the ORR on Ag-based catalysts since it is related to the adsorption of rate-limiting intermediates. Thus, all underlying metals besides Co induce changes in Ag electronic structure (either by strain and ligand effects or generating surface defects) that result in an improved ORR intrinsic activity. In CoAg, however, an upshift of Ag $3d_{5/2}$ can be explained in terms of surface strain since Co may induce changes in the lattice of the overlying Ag film and thus change the electronic structure of surface Ag atoms. The effect of the underlying metal is further evidenced by the lack of correlation in CVs + ORR samples. For these samples, the electronic effects induced by the alloying metal on surface Ag is weakened due to the rather thicker Ag overlayer, as observed in the binding energy shift in CuAg CVs + ORR, which becomes closer to that of pure Ag. For the same reason, since the Ag overlayer thickness is rather stable in AuAg and FeAg samples, they do not exhibit a significant change in their binding energies compared to ORR samples. In CoAg CVs + ORR, instead, we attribute the opposite shift to a different reorganization of surface Ag atoms that results in an inverse strain.

In principle, the correlation in Figure 5a could explain the enhanced activities observed for both CuAg and AuAg because a downshift in Ag binding energy could indicate the upshift of its d-band center closer to the Fermi level, which increases Ag electron density and thus boosts ORR performance by enhancing the kinetics of the O−O bond breakage and promoting the OH^- desorption. Moreover, the decrease in Ag binding energy is in good accordance with the downshift observed in both Cu^0 and Au^0, which could suggest a charge donation from this metal to Ag, thereby resulting in a d-band upshift. However, potential cycling up to 1.5 V_{RHE} reveals different oxygen affinities on these surfaces (Figure 5b). For CuAg, the reduction potential of surface Ag oxides shifts negatively by 41 mV with respect to pure Ag, which indicates a

https://doi.org/10.1021/acsaem.3c00233
ACS Appl. Energy Mater. 2023, 6, 6428−6442

stronger adsorbed-oxygen interaction with Ag surface sites and is therefore in good agreement with its superior performance with respect to pure Ag. It should also be mentioned that this does not rule out the existence of ensemble effects, since Cu 2p spectra reveal a downshift of its d-band, which would also enhance its ORR kinetics through ensemble effects that provide sites for an optimal O_2 adsorption. For AuAg, instead, a positive shift of 37 mV in the Ag reduction peak suggests that Au weakens the oxygen affinity of Ag, which in principle would be contradictive with its improved ORR kinetics considering its RDS is the O_2 dissociative adsorption. This is, in effect, proving that the reason for the enhancement in AuAg is its defect-rich surface with a significant amount of Ag atoms with a low coordination number. Ag atoms placed in these catalytically active sites possess a narrower d-band and thus shifted upward, which results in a more active interaction with adsorbents. In this way, it is possible that the kinetics on AuAg became such that the rate of the reaction is no longer governed by the initial rate of OOH formation but by the OH^- desorption in under-coordinated Ag atoms. Hence, a weaker oxygen affinity in these structural defects has a beneficial effect on its ORR kinetics, which has been shown before in this system.[69] Moreover, although it is plausible that the RDS changes in the same reaction path due to the applied potential, the different electrochemical behavior of CuAg and AuAg is in good agreement with the different Tafel slopes observed in Figure 2e.

The different electronic structure of surface Ag in AuAg is further evidenced by the features observed in the inset of Figure 5b. Since it was concluded that the $4e^-$ pathway is dominant on these surfaces, cycling up to 1.1 V_{RHE} results in the Ag^+/Ag transition in the cathodic region, which is accompanied by the OH^- desorption ($AgOH + e^- = Ag + OH^-$).[38] Thus, although Ag exhibits larger cathodic currents due to the larger amount of Ag, the positive shift of the Ag reduction peak in AuAg implies the stronger desorption of OH^- over AuAg despite the presumably larger OH^- adsorption of the latest. The difference between positive- and negative-going potential sweeps, i.e., hysteresis, is also indicative of the OH^- reversibility because it arises from an additional overpotential required to remove active-site blocking OH_{ads} species in the cathodic scan (Figure 5c). Thus, although single-crystal Ag is known the exhibit a lack of hysteresis because of its reversible OH^- adsorption,[13] both Ag and AuAg samples show hysteresis in our measurements, thereby indicating the stronger OH^- irreversibility on our samples due to surface defects. In CuAg, instead, the observed hysteresis most likely arises from the Cu^0, which is the only active Cu species for the ORR[24] and confirms the role of Cu in actively catalyzing the ORR in this sample. Even though XRD peak assignation is very difficult in AuAg samples due to the very similar lattice parameters of Au and Ag (0.408 nm vs 0.409 nm), the (111) peak characteristic of the fcc structure was observed for both AuAg and Ag samples (Figure 5d). Regardless of which element gives rise to this peak, a negative shift of 0.11° is observed in AuAg ORR samples. This indicates a tensile strain in AuAg ORR of 0.15% with respect to AuAg, which demonstrates the intermixing between Au and Ag and therefore the alloy formation.

Taken together, the results presented in this work support the picture of a potentially beneficial effect on the activity of Ag resulting from the addition of a second metal. We demonstrated that, although Co does not result in improved ORR specific activity due to insufficient alloying, Cu, Fe, and Au hold great potential to boost the activity of Ag active sites. These metals improve the activity of Ag through mechanisms of different nature, which in turn depend on both surface composition and potential region. Although we report a rather strong correlation between Ag ORR activity and its electronic structure in the bimetallic system, we also observed that in some systems the character of the increased activity seems to have an influence on the RDS, which is variant depending on the surface electronic and structural conditions. Hence, due to the highly potential- and surface-dependent ORR mechanism on Ag surfaces, great caution is advised when designing bimetallic or ternary Ag systems that could eventually result in an enhanced ORR activity in alkaline media. Moreover, it should be mentioned that in a real fuel cell, the catalyst will most likely be in the form of nanoparticles, where different alloys can reintroduction of morphology effects that we have tried to avoid in this study.

CONCLUSIONS

In this study, Ag-based bimetallic thin films were fabricated by physical vapor deposition and tested for their ORR performance in alkaline media. The effect of surface composition and electronic structure was investigated, with CuAg exhibiting an over 2-fold ORR specific activity enhancement vs pure Ag at 0.80 V_{RHE}. The improved ORR kinetics on this surface was further demonstrated by its Tafel slope of 27 mV/dec at low overpotentials, even though at this potential region all samples showed improved ORR kinetics with respect to Ag. At higher overpotentials, however, Ag exhibited a faster ORR mechanism that was only surpassed by CuAg and equaled by AuAg, which also exhibited an improved ORR specific activity. However, CuAg and AuAg samples exhibited different responses to potential cycling, which in turn resulted in enhancements of different origin. Although the higher activity of the bimetallic CuAg surface was attributed to both ligand and ensemble effects that result in an optimal bifunctional effect, the better ORR performance on the Ag-rich surface of AuAg was ascribed to the increased presence of undercoordinated Ag atoms with improved O_{ad} due to the underlying Au, whose influence was corroborated by means of XRD. The reversibility of OH_{ad} was further proved by the hysteresis observed in CuAg and AuAg samples. For FeAg and CoAg samples, instead, the insufficient degree of alloying was attributed to be the reason behind the weak improvement in Ag intrinsic activity. Thus, we infer that a greater degree of alloying between Ag and other 3d metals has the potential to result in even more active ORR catalyst. More importantly, ligand effects observed in Ag-based catalysts were found to be highly surface- and potential-dependent, as well as the ORR mechanism, which is required to be elucidated in order to achieve highly effective Ag-based cathode materials.

ASSOCIATED CONTENT

Supporting Information

The Supporting Information is available free of charge at https://pubs.acs.org/doi/10.1021/acsaem.3c00233.

Total surface area from capacitance measurements, cyclic voltammograms of pure metals, calculation of thin film thickness, ORR specific and geometric polarization curves of CVs + ORR samples, peroxide formation plots and electron transfer coefficients of all samples, Koutecky–Levich plots, and calculation of strain from X-ray diffraction spectra (PDF)

https://doi.org/10.1021/acsaem.3c00233
ACS Appl. Energy Mater. 2023, 6, 6428−6442

AUTHOR INFORMATION

Corresponding Authors

Gerard Montserrat-Sisó − *Division of Chemical Physics, Department of Physics and Competence Centre for Catalysis, Chalmers University of Technology, SE-412 96 Gothenburg, Sweden;* orcid.org/0000-0002-3958-7334; Email: gerard.siso@chalmers.se

Björn Wickman − *Division of Chemical Physics, Department of Physics and Competence Centre for Catalysis, Chalmers University of Technology, SE-412 96 Gothenburg, Sweden;* orcid.org/0000-0001-7119-9529; Email: bjorn.wickman@chalmers.se

Complete contact information is available at: https://pubs.acs.org/10.1021/acsaem.3c00233

Notes

The authors declare no competing financial interest.

ACKNOWLEDGMENTS

This project was financially supported by the Swedish Foundation for Strategic Research (Project No. EM16-0060) and the Swedish Research Council (Project No. 2018-03927). The Competence Centre for Catalysis is hosted by Chalmers University of Technology and financially supported by the Swedish Energy Agency (Project No. 52689-1) and the member companies Johnson Matthey, Perstorp, Powercell, Preem, Scania CV, Umicore, and Volvo Group. Sample fabrication was performed in part at Myfab clean room at Chalmers. The authors thank Professor Henrik Grönbeck for valuable discussions and input. The authors also thank Chalmers Materials Analysis Laboratory (CMAL) for part of the physical characterization.

REFERENCES

(1) Bareiß, K.; de la Rua, C.; Möckl, M.; Hamacher, T. Life Cycle Assessment of Hydrogen from Proton Exchange Membrane Water Electrolysis in Future Energy Systems. *Appl. Energy* **2019**, *237*, 862−872.

(2) Ahmadi, P.; Raeesi, M.; Changizian, S.; Teimouri, A.; Khoshnevisan, A. Lifecycle Assessment of Diesel, Diesel-Electric and Hydrogen Fuel Cell Transit Buses with Fuel Cell Degradation and Battery Aging Using Machine Learning Techniques. *Energy* **2022**, *259*, No. 125003.

(3) Stephens, I. E. L.; Bondarenko, A. S.; Grønbjerg, U.; Rossmeisl, J.; Chorkendorff, I. Understanding the Electrocatalysis of Oxygen Reduction on Platinum and Its Alloys. *Energy Environ. Sci.* **2012**, *5*, 6744−6762.

(4) Campos-Roldán, C. A.; Jones, D. J.; Rozière, J.; Cavaliere, S. Platinum-Rare Earth Alloy Electrocatalysts for the Oxygen Reduction Reaction: A Brief Overview. *ChemCatChem* **2022**, *14*, No. e2200334.

(5) Eriksson, B.; Montserrat-Sisó, G.; Brown, R.; Skála, T.; Wreland Lindström, R.; Lindbergh, G.; Wickman, B.; Lagergren, C. Enhanced Oxygen Reduction Activity with Rare Earth Metal Alloy Catalysts in Proton Exchange Membrane Fuel Cells. *Electrochim. Acta* **2021**, *387*, No. 138454.

(6) Kabir, S.; Van Cleve, T.; Khandavalli, S.; Medina, S.; Pylypenko, S.; Mauger, S.; Ulsh, M.; Neyerlin, K. C. Toward Optimizing Electrospun Nanofiber Fuel Cell Catalyst Layers: Microstructure and Pt Accessibility. *ACS Appl. Energy Mater.* **2021**, *4*, 3341−3351.

(7) Jin, H.; Guo, C.; Liu, X.; Liu, J.; Vasileff, A.; Jiao, Y.; Zheng, Y.; Qiao, S. Z. Emerging Two-Dimensional Nanomaterials for Electrocatalysis. *Chem. Rev.* **2018**, *118*, 6337−6408.

(8) Goswami, C.; Hazarika, K. K.; Bharali, P. Transition Metal Oxide Nanocatalysts for Oxygen Reduction Reaction. *Mater. Sci. Energy Technol.* **2018**, *1*, 117−128.

(9) Liu, M.; Xiao, X.; Li, Q.; Luo, L.; Ding, M.; Zhang, B.; Li, Y.; Zou, J.; Jiang, B. Recent Progress of Electrocatalysts for Oxygen Reduction in Fuel Cells. *J. Colloid Interface Sci.* **2022**, *607*, 791−815.

(10) Setzler, B. P.; Zhuang, Z.; Wittkopf, J. A.; Yan, Y. Activity Targets for Nanostructured Platinum-Group-Metal-Free Catalysts in Hydroxide Exchange Membrane Fuel Cells. *Nat. Nanotechnol.* **2016**, *11*, 1020−1025.

(11) Xie, X.; Wei, M.; Du, L.; Nie, Y.; Qi, X.; Shao, Y.; Wei, Z. Enhancement in Kinetics of the Oxygen Reduction on a Silver Catalyst by Introduction of Interlaces and Defect-Rich Facets. *J. Mater. Chem. A* **2017**, *5*, 15390−15394.

(12) Erikson, H.; Sarapuu, A.; Tammeveski, K. Oxygen Reduction Reaction on Silver Catalysts in Alkaline Media: A Minireview. *ChemElectroChem* **2019**, *6*, 73−86.

(13) Blizanac, B. B.; Ross, P. N.; Marković, N. M. Oxygen Reduction on Silver Low-Index Single-Crystal Surfaces in Alkaline Solution: Rotating Ring DiskAg(Hkl) Studies. *J. Phys. Chem. B* **2006**, *110*, 4735−4741.

(14) Zhou, Y.; Lu, Q.; Zhuang, Z.; Hutchings, G. S.; Kattel, S.; Yan, Y.; Chen, J. G.; Xiao, J. Q.; Jiao, F. Oxygen Reduction at Very Low Overpotential on Nanoporous Ag Catalysts. *Adv. Energy Mater.* **2015**, *5*, No. 1500149.

(15) Garlyyev, B.; Liang, Y.; Butt, F. K.; Bandarenka, A. S. Engineering of Highly Active Silver Nanoparticles for Oxygen Electroreduction via Simultaneous Control over Their Shape and Size. *Adv. Sustainable Syst.* **2017**, *1*, No. 1700117.

(16) Jin, Y.; Chen, F.; Lei, Y.; Wu, X. A Silver-Copper Alloy as an Oxygen Reduction Electrocatalyst for an Advanced Zinc-Air Battery. *ChemCatChem* **2015**, *7*, 2377−2383.

(17) Valinton, J. A. A.; Chung, M. C.; Chen, C. H. Laser-Accelerated Mass Transport in Oxygen Reduction Via a Graphene-Supported Silver-Iron Oxide Heterojunction. *J. Phys. Chem. Lett.* **2022**, *13*, 4200−4206.

(18) Wu, X.; Chen, F.; Zhang, N.; Qaseem, A.; Johnston, R. L. Engineering Bimetallic Ag − Cu Nanoalloys for Highly Efficient Oxygen Reduction Catalysts: A Guideline for Designing Ag-Based Electrocatalysts with Activity Comparable to Pt/C-20%. *Small* **2017**, *13*, No. 1603876.

(19) Wang, Q.; Chen, F.; Liu, Y.; Gebremariam, T. T.; Wang, J.; An, L.; Johnston, R. L. AgSn Intermetallics as Highly Selective and Active Oxygen Reduction Electrocatalysts in Membraneless Alkaline Fuel Cells. *J. Power Sources* **2018**, *404*, 106−117.

(20) Wu, X.; Chen, F.; Zhang, N.; Lei, Y.; Jin, Y.; Qaseem, A.; Johnston, R. L. Activity Trends of Binary Silver Alloy Nanocatalysts for Oxygen Reduction Reaction in Alkaline Media. *Small* **2017**, *13*, No. 1603387.

(21) Yang, Y.; Montserrat-Sisó, G.; Wickman, B.; Nikolaychuk, P. A.; Soroka, I. L. Core-Shell and Heterostructured Silver-Nickel Nanocatalysts Fabricated by γ-Radiation Induced Synthesis for Oxygen Reduction in Alkaline Media. *Dalton Trans.* **2022**, *51*, 3604−3615.

(22) Qaseem, A.; Chen, F.; Wu, X.; Johnston, R. L. Pt-Free Silver Nanoalloy Electrocatalysts for Oxygen Reduction Reaction in Alkaline Media. *Catal. Sci. Technol.* **2016**, *6*, 3317−3340.

(23) Vega-Cartagena, M.; Flores-Vélez, E. M.; Colón-Quintana, G. S.; Blasini Pérez, D. A.; De Jesús, M. A.; Cabrera, C. R. Silver-Palladium Electrodeposition on Unsupported Vulcan XC-72R for Oxygen Reduction Reaction in Alkaline Media. *ACS Appl. Energy Mater.* **2019**, *2*, 4664−4673.

(24) Higgins, D.; Wette, M.; Gibbons, B. M.; Siahrostami, S.; Hahn, C.; Escudero-Escribano, M.; García-Melchor, M.; Ulissi, Z.; Davis, R. C.; Mehta, A.; Clemens, B. M.; Nørskov, J. K.; Jaramillo, T. F. Copper Silver Thin Films with Metastable Miscibility for Oxygen Reduction Electrocatalysis in Alkaline Electrolytes. *ACS Appl. Energy Mater.* **2018**, *1*, 1990−1999.

(25) Holewinski, A.; Idrobo, J. C.; Linic, S. High-Performance Ag-Co Alloy Catalysts for Electrochemical Oxygen Reduction. *Nat. Chem.* **2014**, *6*, 828−834.

(26) Hammer, B.; Nørskov, J. K. Electronic Factors Determining the Reactivity of Metal Surfaces. *Surf. Sci.* **1995**, *343*, 211−220.

(27) Yang, X.; Gan, L.; Zhu, C.; Lou, B.; Han, L.; Wang, J.; Wang, E. A Dramatic Platform for Oxygen Reduction Reaction Based on Silver Nanoclusters. *Chem. Commun.* **2014**, *50*, 234−236.
(28) Nørskov, J. K.; Rossmeisl, J.; Logadottir, A.; Lindqvist, L.; Kitchin, J. R.; Bligaard, T.; Jónsson, H. Origin of the Overpotential for Oxygen Reduction at a Fuel-Cell Cathode. *J. Phys. Chem. B* **2004**, *108*, 17886−17892.
(29) Singh, P.; Buttry, D. A. Comparison of Oxygen Reduction Reaction at Silver Nanoparticles and Polycrystalline Silver Electrodes in Alkaline Solution. *J. Phys. Chem. C* **2012**, *116*, 10656−10663.
(30) Jiang, K.; Zhang, H. X.; Zou, S.; Cai, W. Bin. Electrocatalysis of Formic Acid on Palladium and Platinum Surfaces: From Fundamental Mechanisms to Fuel Cell Applications. *Phys. Chem. Chem. Phys.* **2014**, *16*, 20360−20376.
(31) Hu, S.; Goenaga, G.; Melton, C.; Zawodzinski, T. A.; Mukherjee, D. PtCo/CoOx Nanocomposites: Bifunctional Electrocatalysts for Oxygen Reduction and Evolution Reactions Synthesized via Tandem Laser Ablation Synthesis in Solution-Galvanic Replacement Reactions. *Appl. Catal., B* **2016**, *182*, 286−296.
(32) Mehar, V.; Almithn, A.; Egle, T.; Yu, M. H.; O'Connor, C. R.; Karatok, M.; Madix, R. J.; Hibbitts, D.; Weaver, J. F. Oxophilicity Drives Oxygen Transfer at a Palladium-Silver Interface for Increased CO Oxidation Activity. *ACS Catal.* **2020**, *10*, 13878−13889.
(33) Sato, Y.; Taketomo, M.; Ito, N.; Miyamura, A.; Shigesato, Y. Comparative Study on Early Stages of Film Growth for Transparent Conductive Oxide Films Deposited by Dc Magnetron Sputtering. *Thin Solid Films* **2008**, *516*, 4598−4602.
(34) Campos-Roldán, C. A.; González-Huerta, R. G.; Alonso-Vante, N. Experimental Protocol for HOR and ORR in Alkaline Electrochemical Measurements. *J. Electrochem. Soc.* **2018**, *165*, J3001−J3007.
(35) Wei, C.; Rao, R. R.; Peng, J.; Huang, B.; Stephens, I. E. L.; Risch, M.; Xu, Z. J.; Shao-Horn, Y. Recommended Practices and Benchmark Activity for Hydrogen and Oxygen Electrocatalysis in Water Splitting and Fuel Cells. *Adv. Mater.* **2019**, *31*, No. 1806296.
(36) Gasteiger, H. A.; Kocha, S. S.; Sompalli, B.; Wagner, F. T. Activity Benchmarks and Requirements for Pt, Pt-Alloy, and Non-Pt Oxygen Reduction Catalysts for PEMFCs. *Appl. Catal., B* **2005**, *56*, 9−35.
(37) Yu, L.; Akolkar, R. Lead Underpotential Deposition for the Surface Characterization of Silver Ad-Atom Modified Gold Electrocatalysts for Glucose Oxidation. *J. Electroanal. Chem.* **2017**, *792*, 61−65.
(38) He, F.; Xia, N.; Zheng, Y.; Fan, H.; Ma, D.; Hu, X. Boosting Oxygen Electroreduction over Strained Silver. *ACS Appl. Mater. Interfaces* **2020**, *12*, 57134−57140.
(39) Van Cleve, T.; Gibara, E.; Linic, S. Electrochemical Oxygen Reduction Reaction on Ag Nanoparticles of Different Shapes. *ChemCatChem* **2016**, *8*, 256−261.
(40) Giri, S. D.; Sarkar, A. Estimating Surface Area of Copper Powder: A Comparison between Electrochemical, Microscopy and Laser Diffraction Methods. *Adv. Powder Technol.* **2018**, *29*, 3520−3526.
(41) Huck-Iriart, C.; Soler, L.; Casanovas, A.; Marini, C.; Prat, J.; Llorca, J.; Escudero, C. Unraveling the Chemical State of Cobalt in Co-Based Catalysts during Ethanol Steam Reforming: An in Situ Study by Near Ambient Pressure XPS and XANES. *ACS Catal.* **2018**, *8*, 9625−9636.
(42) Huang, C.; Zheng, L.; Feng, W.; Guo, A.; Gao, X.; Long, Z.; Qiu, X. Copper Isolated Sites on N-Doped Carbon Nanoframes for Efficient Oxygen Reduction. *ACS Sustainable Chem. Eng.* **2020**, *8*, 14030−14038.
(43) Klyushin, A. Y.; Rocha, T. C. R.; Hävecker, M.; Knop-Gericke, A.; Schlögl, R. A near Ambient Pressure XPS Study of Au Oxidation. *Phys. Chem. Chem. Phys.* **2014**, *16*, 7881−7886.
(44) Liu, L.; Li, W.; Xiong, Z.; Xia, D.; Yang, C.; Wang, W.; Sun, Y. Synergistic Effect of Iron and Copper Oxides on the Formation of Persistent Chlorinated Aromatics in Iron Ore Sintering Based on in Situ XPS Analysis. *J. Hazard. Mater.* **2019**, *366*, 202−209.
(45) Guo, J.; Hsu, A.; Chu, D.; Chen, R. Improving Oxygen Reduction Reaction Activities on Carbon-Supported Ag Nanoparticles in Alkaline Solutions. *J. Phys. Chem. C* **2010**, *114*, 4324−4330.
(46) Xie, R. C.; Batchelor-McAuley, C.; Rauwel, E.; Rauwel, P.; Compton, R. G. Electrochemical Characterisation of Co@Co(OH)2 Core-Shell Nanoparticles and Their Aggregation in Solution. *ChemElectroChem* **2020**, *7*, 4259−4268.
(47) Silva Olaya, A. R.; Zandersons, B.; Wittstock, G. Restructuring of Nanoporous Gold Surfaces During Electrochemical Cycling in Acidic and Alkaline Media. *ChemElectroChem* **2020**, *7*, 3670−3678.
(48) Štrbac, S.; Srejić, I.; Rakočević, Z. Catalysis of Oxygen Reduction on Electrochemically Activated Polycrystalline Gold by Pd Nanoislands in Alkaline Solution. *J. Electroanal. Chem.* **2017**, *789*, 76−84.
(49) Štrbac, S.; Adžić, R. R. The Influence of OH- Chemisorption on the Catalytic Properties of Gold Single Crystal Surfaces for Oxygen Reduction in Alkaline Solutions. *J. Electroanal. Chem.* **1996**, *403*, 169−181.
(50) Bülter, H.; Denuault, G.; Máté, S.; Máté, M.; Dosche, C.; Wittstock, G. Electrochemical Analysis of Nanostructured Iron Oxides Using Cyclic Voltammetry and Scanning Electrochemical Microscopy. *Electrochim. Acta* **2016**, *222*, 1326−1334.
(51) Zeledón, J. A. Z.; Kreider, M. E.; Ben-naim, M.; Hubert, M. A.; Avile, J. E.; Nørskov, J. K.; Stevens, M. B.; Jaramillo, T. F.; et al. Engineering Metal−Metal Oxide Surfaces for High-Performance Oxygen Reduction on Ag−Mn Electrocatalysts. *Energy Environ. Sci.* **2022**, *15*, 1611−1629.
(52) Betancourt, L. E.; Rojas-Pérez, A.; Orozco, I.; Frenkel, A. I.; Li, Y.; Sasaki, K.; Senanayake, S. D.; Cabrera, C. R. Enhancing ORR Performance of Bimetallic PdAg Electrocatalysts by Designing Interactions between Pd and Ag. *ACS Appl. Energy Mater.* **2020**, *3*, 2342−2349.
(53) Vitos, L.; Ruban, A. V.; Skriver, H. L.; Kolla, J. The Surface Energy of Metals. *Surf. Sci.* **1998**, *411*, 186−202.
(54) Stein, F.; Kohsakowski, S.; Martinez, R.; Reichenberger, S.; Rehbock, C.; Colic, V. Disproportional Surface Segregation in Ligand-Free Gold − Silver Alloy Solid Solution Nanoparticles, and Its Implication for Catalysis and Biomedicine. *Faraday Discuss.* **2022**, *242*, 301−325.
(55) Park, Y.; Shin, K.; Lee, C.; Lee, S.; Lee, Y.; Kim, C.; Cho, H.; Henkelman, G.; Mo, H. Iterative Redox Activation Promotes Interfacial Synergy in an Ag/Cu_xO Catalyst for Oxygen Reduction. *Chem. Eng. J.* **2022**, *446*, No. 136966.
(56) Agrawal, K.; Naik, A.; Chaudhary, S.; Parvatalu, D. Prudent Practices in Ex Situ Durability Analysis Using Cyclic Voltammetry for Platinum-Based Electrocatalysts. *Chem. − Asian J.* **2021**, *16*, 3311−3325.
(57) Xiong, L.; Sun, Z.; Zhang, X.; Zhao, L.; Huang, P.; Chen, X.; Jin, H.; Sun, H.; Lian, Y.; Deng, Z.; Rümmerli, M. H.; Yin, W.; Zhang, D.; Wang, S.; Peng, Y. Octahedral Gold-Silver Nanoframes with Rich Crystalline Defects for Efficient Methanol Oxidation Manifesting a CO-Promoting Effect. *Nat. Commun.* **2019**, *10*, No. 3782.
(58) Shinagawa, T.; Garcia-Esparza, A. T.; Takanabe, K. Insight on Tafel Slopes from a Microkinetic Analysis of Aqueous Electrocatalysis for Energy Conversion. *Sci. Rep.* **2015**, *5*, No. 13801.
(59) Linge, J. M.; Erikson, H.; Kasikov, A.; Rähn, M.; Sammelselg, V.; Tammeveski, K. Oxygen Reduction Reaction on Thin-Film Ag Electrodes in Alkaline Solution. *Electrochim. Acta* **2019**, *325*, No. 134922.
(60) Fletcher, S. Tafel Slopes from First Principles. *J. Solid State Electrochem.* **2009**, *13*, 537−549.
(61) Marković, N. M.; Gasteiger, H. A.; Ross, P. N. Oxygen Reduction on Platinum Low-Index Single-Crystal Surfaces in Alkaline Solution: Rotating Ring DiskPt(Hkl) Studies. *J. Phys. Chem. A* **1996**, *100*, 6715−6721.
(62) Lima, F. H. B.; de Castro, J. F. R.; Ticianelli, E. A. Silver-Cobalt Bimetallic Particles for Oxygen Reduction in Alkaline Media. *J. Power Sources* **2006**, *161*, 806−812.
(63) Hernández-Rodríguez, M.; Goya, M. C.; Arévalo, M. C.; Rodríguez, J. L.; Pastor, E. Carbon Supported Ag and Ag−Co Catalysts Tolerant to Methanol and Ethanol for the Oxygen Reduction Reaction in Alkaline Media. *Int. J. Hydrogen Energy* **2016**, *41*, 19789−19798.
(64) Gibbons, B. M.; Wette, M.; Stevens, M. B.; Davis, R. C.; Siahrostami, S.; Kreider, M.; Mehta, A.; Higgins, D. C.; Clemens, B. M.; Jaramillo, T. F. In Situ X-Ray Absorption Spectroscopy Disentangles

https://doi.org/10.1021/acsaem.3c00233
ACS Appl. Energy Mater. 2023, 6, 6428−6442

the Roles of Copper and Silver in a Bimetallic Catalyst for the Oxygen Reduction Reaction. *Chem. Mater.* **2020**, *32*, 1819−1827.
(65) Li, R.; Xu, J.; Zeng, R.; Pan, Q.; Tang, T.; Luo, W. Halides-Assisted Electrochemical Synthesis of Cu/Cu2O/CuO Core-Shell Electrocatalyst for Oxygen Evolution Reaction. *J. Power Sources* **2020**, *457*, No. 228058.
(66) Balkan, T.; Küçükkeçeci, H.; Zarenezhad, H.; Kaya, S. One-Pot Synthesis of Monodisperse Copper e Silver Alloy Nanoparticles and Their Composition-Dependent Electrocatalytic Activity for Oxygen Reduction Reaction. *J. Alloys Compd.* **2020**, *831*, No. 154787.
(67) Kutluk, G.; Nakatake, M.; Sumida, H.; Namatame, H.; Taniguchi, M.; et al. Electronic Structure of Supported Metal Nanoparticles. *AIP Conf. Proc.* **2010**, *1234*, 923−926.
(68) Miller, H. A.; Bevilacqua, M.; Filippi, J.; Lavacchi, A.; Marchionni, A.; Marelli, M.; Moneti, S.; Oberhauser, W.; Vesselli, E.; Innocenti, M.; Vizza, F. Nanostructured Fe-Ag Electrocatalysts for the Oxygen Reduction Reaction in Alkaline Media. *J. Mater. Chem. A* **2013**, *1*, 13337−13347.
(69) Wang, J.; Chen, F.; Jin, Y.; Lei, Y. Dilute Au-Containing Ag Nanosponges as a Highly Active and Durable Electrocatalyst for Oxygen Reduction and Alcohol Oxidation Reactions. *ACS Appl. Mater. Interfaces* **2018**, *10*, 6276−6287.

https://doi.org/10.1021/acsaem.3c00233
ACS Appl. Energy Mater. 2023, 6, 6428−6442